# Engineering oxygen vacancies in hierarchically Li-rich layered oxide porous microspheres for high-rate lithium ion battery cathode

Yuxin Cai[1], Lun Ku[1], Laisen Wang[1*], Yating Ma[1], Hongfei Zheng[1], Wanjie Xu[1], Jiangtao Han[1], Baihua Qu[2], Yuanzhi Chen[1], Qingshui Xie[1*] and Dong-Liang Peng[1*]

**ABSTRACT**   Lithium-rich layered oxides always suffer from low initial Coulombic efficiency, poor rate capability and rapid voltage fading. Herein, engineering oxygen vacancies in hierarchically $Li_{1.2}Mn_{0.54}Ni_{0.13}Co_{0.13}O_2$ porous microspheres (L@S) is carried out to suppress the formation of irreversible $Li_2O$ during the initial discharge process and improve the $Li^+$ diffusion kinetics and structural stability of the cathode mateiral. As a result, the prepared L@S cathode delivers high initial Coulombic efficiency of 92.3% and large specific capacity of 292.6 mA h g$^{-1}$ at 0.1 C. More importantly, a large reversible capacity of 222 mA h g$^{-1}$ with a capacity retention of 95.7% can be obtained after 100 cycles at 10 C. Even cycled at ultrahigh rate of 20 C, the L@S cathode can deliver stable reversible capacity of 153 mA h g$^{-1}$ after 100 cycles. Moreover, the full cell using L@S as cathode and $Li_4Ti_5O_{12}$ as anode exhibits a relatively high reversible capacity of 141 mA h g$^{-1}$ with an outstanding voltage retention of 97% after 400 cycles at a large current density of 3 C. These results may shed light on the improvement of electrochemical performances of lithium-rich layered oxides *via* the multiscale coordinated design based on atomic defects, microstructure and composition.

**Keywords:** lithium-rich layered cathode, oxygen vacancies, spinel encapsulating layer, hierarchically porous structure, high rate capability

## INTRODUCTION

With the vigorous developement of electric vehicles (EVs), the current cathode materials, such as $LiMn_2O_4$, $LiFePO_4$, $LiCoO_2$ and $LiMO_2$ (M=Ni, Co, Mn, Al, Fe, etc.), are far from satisfying the endurance mileages [1–4].

Recently, lithium-rich layered oxides (LLROs) have received a great deal of attention on account of their large specific capacity and high working potential [5,6]. However, the irreversible release of oxygen on the surface of electrode materials leads to huge phase transition, resulting in low initial Coulombic efficiency, poor cyclic stability and severe voltage decay [7–9]. Besides, the two dimensional (2D) $Li^+$ diffusion tunnels of LLROs lead to inferior rate capability [10]. These features greatly hinder the large-scale commercial application of LLROs in high-performance lithium ion batteries.

Many ways like morphological control, surface modification and defect design have been applied to improve the electrochemical performance of LLROs. Generally, morphological control can shorten the $Li^+$ diffusion paths but not stabilize the surface structure of electrode materials [11–14]. The coating layers, such as metal oxides [15–17], metal phosphates [18], and fluorides [19], help to reduce the dissolution of transition metal ions but decrease the overall reversible capacity for their electrochemical inertness. Liu *et al.* [20] reported that controlling the structural defects of stacking faults could improve the initial reversible capacity of LLROs. But their results still showed poor cycle and rate performances. In addition, oxygen defects were created in the electrode materials to facilitate $Li^+$ diffusion [21,22]. However, the poor rate capability and rigorous experimental conditions both urge us to seek better strategies.

Herein, we put forward a multiscale coordinated design to engineer oxygen vacancies in hierarchically porous $Li_{1.2}Mn_{0.54}Ni_{0.13}Co_{0.13}O_2$ (LMNC) microspheres en-

---

[1] Department of Materials Science and Engineering, State Key Lab of Physical Chemistry of Solid Surface, Collaborative Innovation Center of Chemistry for Energy Materials, College of Materials, Xiamen University, Xiamen 361005, China
[2] Pen-Tung Sah Institute of Micro-Nano Science and Technology, Xiamen University, Xiamen 361005, China
* Corresponding authors (emails: wangls@xmu.edu.cn (Wang L); xieqsh@xmu.edu.cn (Xie Q); dlpeng@xmu.edu.cn (Peng DL))

capsulated by surface spinel layer (L@S). This design based on atomic defects, microstructure and composition possesses the following functions: 1) the surface oxygen vacancies help to pre-activate $Li_2MnO_3$ phase, reduce the energy barrier of $Li^+$ diffusion and then enhance $Li^+$ diffusion rate; 2) the *in-situ* formed surface spinel encapsulating layer with 3D $Li^+$ diffusion channels can stabilize the surface structure and facilitate rapid $Li^+$ transportation; 3) the hierarchically porous structure can shorten $Li^+$ diffusion paths. As a result, the elaborately designed L@S microspheres deliver greatly improved electrochemical performances in terms of extremely high initial Coulombic efficiency, large specific capacity, outstanding high-rate long-term cyclability and voltage stability.

## EXPERIMENTAL SECTION

### Synthesis of the hierarchically porous LMNC microspheres
The layered lithium-rich manganese-based oxide (LMNC) microspheres were prepared through a solvothermal method, followed by a two-step calcination process, as shown in Fig. S1. All the reagents used are of analytical grade. Typically, $Mn(CH_3COO)_2 \cdot 4H_2O$ (3.2 mmol), $Ni(CH_3COO)_2 \cdot 4H_2O$ (0.8 mmol) and $Co(CH_3COO)_2 \cdot 4H_2O$ (0.8 mmol) were dissolved in 48 mL of ethylene glycol under sonication. One gram of polyvinylpyrrolidone (PVP) which would form micelles in ethylene glycol was then added as a structural-direct agent. After being stirred for 30 min, a wine red transparent solution was formed as solution A. At the same time, 24 mmol of $NH_4HCO_3$ was dissolved into the mixture containing 10 mL of deionized water and 16 mL of polyethylene glycol (PEG 600), named solution B. Then, the solution B was added dropwise into solution A to form a uniform solution with continuous stirring for 10 min. Finally, the mixture was transferred to a 100-mL Teflon-lined stainless steel autoclave, which was then sealed without shaking and heated at 180°C for 10 h. After being cooled down to room temperature naturally, the pink precipitate was collected and washed with deionized water and ethanol for several times. The $Mn_{2/3}Ni_{1/6}Co_{1/6}CO_3$ precursor was gained after drying at 60°C. To prepare the Li-rich layered oxide, the precursor was first annealed at 500°C for 5 h. And then the obtained oxide precursor and stoichiometric amounts of $LiOH \cdot H_2O$ (with 5 wt% excess) were evenly dispersed together and sintered at 800°C for 12 h in air at a heating rate of 2°C min$^{-1}$. Finally, the hierarchically porous spherical like LMNC was obtained.

### Synthesis of the layered@spinel heterostructured LMNC microspheres (L@S)
The pristine LMNC (100 mg) and 30 mg of dopamine hydrochloride were added into 60 mL of tris-buffer aqueous solution (10 mmol L$^{-1}$, pH≈8.5), accompanied by a polymerization process of dopamine on the surface of LMNC under continuous stirring for 5 h. After centrifugation and drying, the as-polymerized sample was carbonized at 500°C for 30 min in air at a heating rate of 10°C min$^{-1}$, and the L@S was gained.

### Materials characterization
The crystal phases of the products were characterized by X-ray diffraction (XRD, PANalytical X'pert PRO X-ray diffractometer, Cu Kα radiation 40 kV, 40 mA). Rietveld refinements were carried out by using a General Structure Analysis System (GSAS) software package based on a three-phase model system of *R-3m*, *C2/m* and *Fd-3m*. The field emission scanning electron microscope (FESEM, Hitachi SU-70) and transmission electron microscope (TEM, JEM-2100, 200 kV) were applied to analyze the morphology and microstructure of the samples. The Brunauer-Emmett-Teller (BET) specific surface area and pore size contribution plots were tested by nitrogen adsorption/desorption measurement at 77 K on a 3H-2000PM2 instrument. Thermogravimetric analysis (TGA) and differential scanning calorimetry (DSC) measurements were carried out at a heating rate of 10°C min$^{-1}$ using TGA/DSC analyzer (SDT Q600, TA Instrument). The Raman measurement was performed using an XploRA microprobe Raman system (HORIBA) with a 532 nm excitation line and a 0.1 mW laser power. Chemical valence sate analysis was implemented by X-ray photoelectron spectroscopy (XPS) on PHI QUANTUM 2000 (monochromatic Al K X-ray source). PL measurements were carried out on a fluorescence photometer (HORIBA). UV-vis-NIR spectra were recorded on a Lambda 750 UV-vis-NIR spectrometer (PerkinElmer) in 200–1300 nm. *In situ* XRD experiments were carried out on a D8 Discover X-ray diffractometer. The cells were cycled between 2.0–4.8 V at 0.5 C.

### Electrochemical measurements
The electrochemical performances of the as-synthesized LMNC and L@S samples were investigated by assembling 2025 type coin cells. Specifically, the active materials, acetylene black and polyvinylidene difluoride in the weight ratio of 7:2:1 were mixed in *N*-methyl-2-pyrrolidone (NMP) to form a slurry, which was then scraped uniformly on the aluminum foil and dried at 80°C for

12 h under vacuum condition to obtain the working electrode. The weight loading of the active materials was about 0.8 mg cm$^{-2}$. The metallic lithium foil served as the counter electrode. The Celgard 2400 was used as the separator and the electrolyte was 1 mol L$^{-1}$ LiPF$_6$ in a mixture of ethylene carbonate (EC) and dimethyl carbonate (DMC) with a volume ratio of 1:1. The galvanostatic charge/discharge measurements were performed on the Neware battery program-control system within 2.0–4.8 V at 30°C. Cyclic voltammetry (CV) tests were carried out on the electrochemical workstation (CHI660E) at a scan rate of 0.1 mV s$^{-1}$ in the potential window of 2.0–4.8 V (*vs.* Li/Li$^+$). Electrochemical impedance spectroscopy (EIS) measurements were performed on the above electrochemical workstation with the alternative current (AC) signal amplitude of 5 mV in the frequency range from 100 kHz to 0.01 Hz. The Li$^+$ diffusion coefficients can be calculated according to the following equation:

$$D_{Li^+} = \frac{R^2 T^2}{2A^2 n^4 F^4 C^2 \sigma^2},\qquad(1)$$

where $R$ is the gas constant (8.314 J mol$^{-1}$ K$^{-1}$), $T$ is the absolute temperature (here is 298.15 K), $A$ is the surface area of electrode (1.1304 cm$^2$), $n$ is the number of transferred electrons per molecule during oxidation, $F$ is the Faraday constant (96,485.34 C mol$^{-1}$) and $C$ is the concentration of Li$^+$ (4.96×10$^{-2}$ mol cm$^{-3}$).

## RESULTS AND DISCUSSION

As shown in Fig. S1, the pristine hierarchically porous LMNC materials were synthesized through a solvothermal route, followed by calcination treatment. Then, as shown in Scheme 1, the dopamine layer was formed on the surface of LMNC microspheres by the self-polymerization of dopamine hydrochloride and subsequently subjected to heating treatment. According to the TGA-DSC curves (Fig. S2), the coated dopamine layer was firstly carbonized to form a carbon layer, and then the as-formed carbon layer reacted with the partial lattice oxygen near the surface of LMNC and the oxygen in air to form CO$_2$ gas escaping from the sample. As a result, oxygen vacancies were successfully formed on the surface of L@S cathode material. Simultaneously, the structural rearrangement induced by the oxygen defects on the surface lead to the *in situ* formation of surface spinel encapsulating layer. Consequently, oxygen vacancies-decorated hierarchically porous layered-spinel heterostructured L@S microspheres were successfully prepared.

The N$_2$ adsorption-desorption isotherms of LMNC and L@S at 77 K are shown in Fig. S3. The Brunauer-Emmett-Teller surface areas for LMNC and L@S are 6.2 and

## Multiscale design based on atomic defects, microstructure and composition
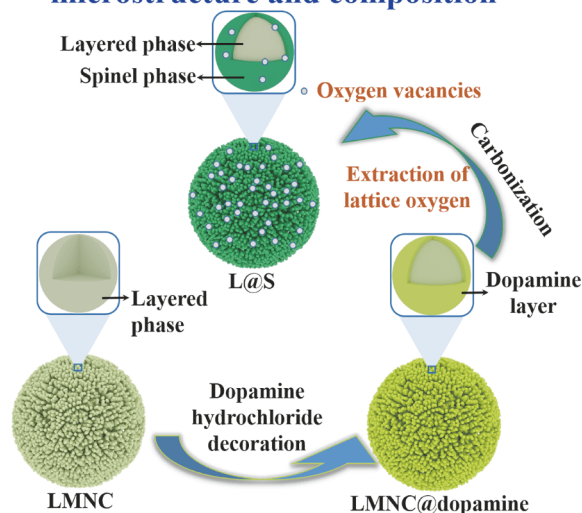


**Scheme 1** Schematic diagram for the engineering of oxygen vacancies into L@S cathode material.

7.2 m$^2$ g$^{-1}$, respectively, which are similar to the reported porous Li-rich cathodes [23]. Moreover, the pore distribution plots were analyzed *via* the Barret-Joyner-Halenda method. The results further prove that both samples possess two pore size distributions at about 3 and 60 nm. In this work, the obtained material is a micro-sized sphere composed of plenty of primary nanoparticles. As the primary particle plays a key role in favorable kinetics of Li$^+$, the micro-sized matrix can improve the structural stability and hinder side reactions, realizing a better cycle durability [11–13].

To confirm the oxygen vacancies in L@S, both LMNC and L@S were characterized by XPS. As shown in Fig. 1a, both samples have Li, Mn, Co, Ni and O, and the C signal may result from the surface contaminant or the test instrument. The binding energies of Ni 2p$_{3/2}$ (Fig. 1b) and Co 2p$_{3/2}$ (Fig. 1c) locate at 855.4 and 780.8 eV, respectively, demonstrating that the elements are in the form of Ni$^{2+}$ and Co$^{3+}$ [10]. In contrast, Mn 2p peaks of L@S negatively shift by 0.5 eV (Fig. 1d), indicating that fewer O atoms neighbor around Mn on average [24]. The binding energy of Mn 2p$_{2/3}$ decreases to 642.1 eV for L@S, which is attributed to the presence of Mn$^{3+}$ and indirectly validates the formation of oxygen vacancies for the charge balance [25,26]. The Mn 2p XPS spectrum of L@S is fitted and shown in Fig. 1e. Specifically, the Mn 2p$_{2/3}$ peaks of Mn$^{3+}$ and Mn$^{4+}$ locate at 641.6 and 642.6 eV. The calculation based on the fitted peak area indicates that the average valence of Mn in L@S reduces from +4 to +3.89.
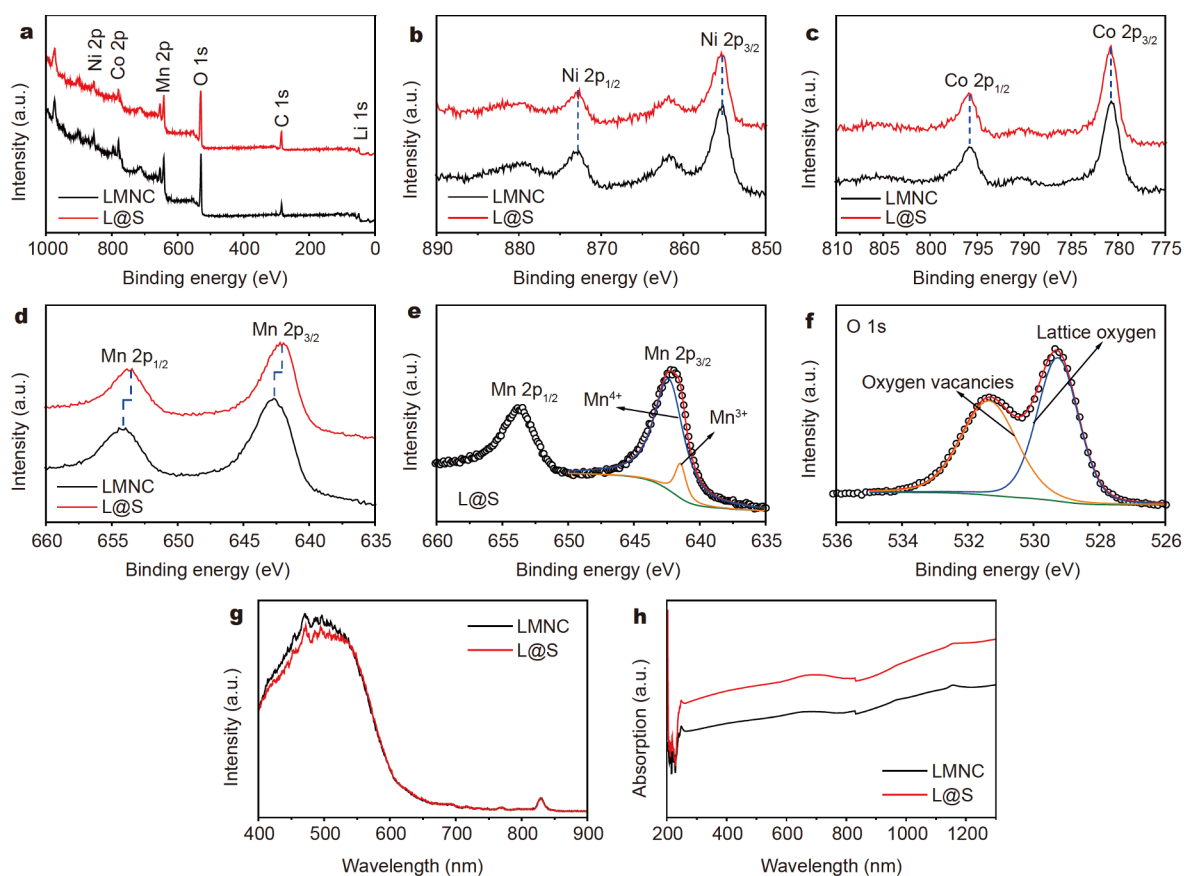
**Figure 1** High-resolution full (a), Ni 2p (b), Co 2p (c) and Mn 2p (d) XPS spectra of LMNC and L@S. The fitting Mn 2p (e) and O 1s (f) XPS spectrum of L@S. Photoluminescence spectra (g), UV-vis-NIR absorption spectra (h) of LMNC and L@S.

Meanwhile, the peak at 531.2 eV of O 1s spectrum also strongly suggests the generation of oxygen vacancies in L@S (Fig. 1f) [27,28]. This result was further proved by photoluminescence spectra and UV-vis-NIR absorption spectra of both samples. The weaker luminescence peak at 490 nm of L@S (Fig. 1g) corresponds to a lower recombination rate of electrons and holes, meaning lower electron concentration caused by oxygen vacancies [29]. As shown in Fig. 1h, compared with LMNC, L@S has an obviously stronger enhanced absorption ability for UV-vis-NIR light, related to oxygen vacancies-induced localized surface plasmon resonance effect [26,30]. Hence, it can be concluded that oxygen vacancies have been introduced into the cathode materials after the reaction between carbon and the partial lattice oxygen atoms on the surface of L@S.

Fig. 2a shows the Raman spectra of the as-prepared LMNC and L@S. Two main peaks around 600 and 476 cm$^{-1}$ are ascribed to A$_{1g}$ stretching and E$_g$ bending of the layered $R$-3$m$ structure. The blue shift of E$_g$ vibrations

in L@S indicates the formation of defects caused by coating [31]. The shoulder peak at 650 cm$^{-1}$ for L@S is attributed to the Mn–O stretching vibrations of the Li$_4$Mn$_5$O$_{12}$ spinel phase [31–33]. Moreover, the main diffraction peaks in XRD patterns are well indexed into the α-NaFeO$_2$-type structure with $R$-3$m$ symmetry for both two samples (Fig. 2b). The weak superlattice reflections from 20° to 25° ascribed to the short-range ordering arrangement of Li and Mn ions in the transition metal layers of the Li$_2$MnO$_3$ are also observed. The distinct split peaks of (006)/(102) and (018)/(110) indicate good layered structure for both samples. Compared with the pristine LMNC, the heterostructured L@S basically maintains the feature of lithium-rich component and layer structure unchanged except for the formation of a small amount of Li$_4$Mn$_5$O$_{12}$ phase, which can be proved by the small bulge near the (003) and (101) peaks in the enlarged XRD pattern in Fig. 2c, d [34]. As shown in Fig. 2e, f and Table S1, the refined results further indicate that the phase fraction of $R$-3$m$, $C2/m$ and $Fd$-3$m$
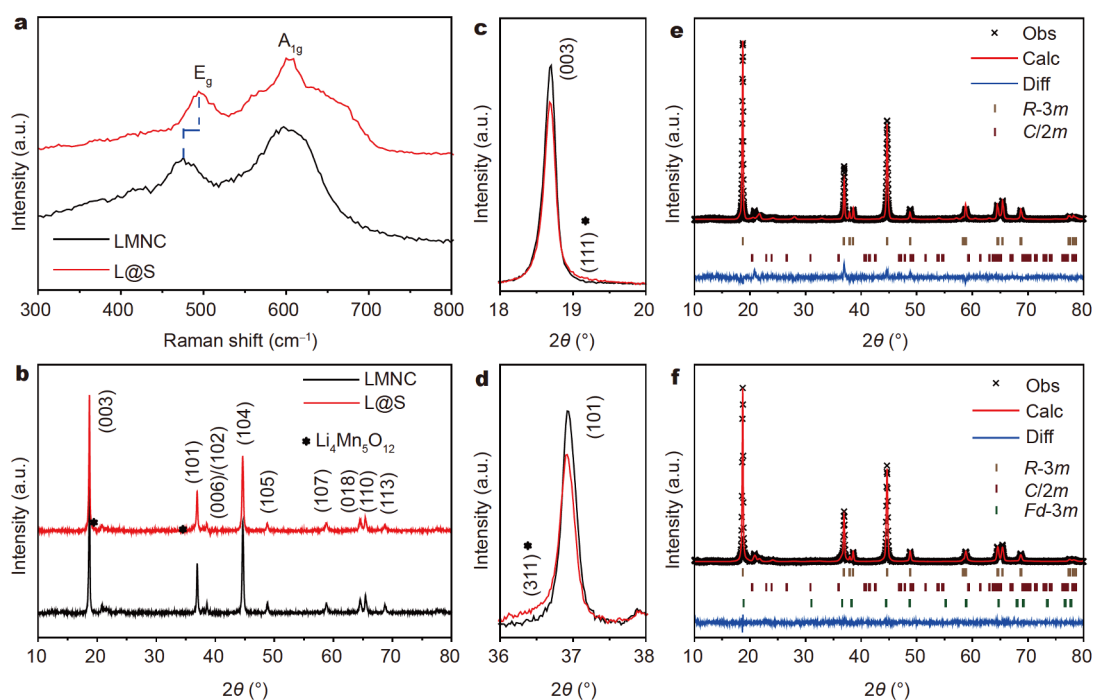
**Figure 2** Raman profiles (a), XRD patterns (b) and corresponding enlarged regions (c, d) in XRD patterns of LMNC and L@S. Rietveld refinements of pristine LMNC (e) and L@S (f).

$Li_4Mn_5O_{12}$ are 58.5, 37.8, and 3.7 wt.%, respectively. Such a phase transition is induced by the generation of oxygen vacancies due to the extraction of surface lattice oxygen [35].

As depicted in Fig. 3a–c and Fig. S4a–d, similar to LMNC, L@S keeps the hierarchically porous quasi-sphere shape unchanged after heating engineering. Only one set of lattice fringe exists on the outer surface of LMNC (Fig. S4e), which can be indexed as (003) plane of α-NaFeO$_2$ structure. The SEM image of LMNC@dopamine sample shows that there is no obvious difference between the samples before and after dopamine coating except for the thin layer coated on the surface of LMNC@dopamine (Fig. S5a). What's more, the TEM image indicates that the thickness of coating layer is about 20 nm (Fig. S5b). And the same lattice fringe to LMNC proves that the dopamine coating has no influence on the structure of microspheres (Fig. S5c). As for L@S, the TEM image (Fig. 3d) and element mappings (Fig. 3i–m and Fig. S5d–i), combined with the TGA-DSC curves and XRD patterns, show that the coated dopamine layer is fully involved in the reaction during heating treatment in air. The diffraction ring assigned to (220) plane in selected area electron diffraction (SAED) pattern (Fig. 3e) verifies the spinel phase. Moreover, a new set of lattice

fringe with interlayer spacing of 0.21 nm referring to (400) plane of $Fd$-$3m$ can be seen (Fig. 3f). These results verify the existence of spinel phase on the surface of L@S caused by the oxygen removal. Additionally, some lattice dislocations (Fig. 3g) and porous tunnels (Fig. 3h) on the surface of L@S microspheres can also be observed, which originate from the extraction of oxygen and migration of transition metal ions after heating treatment [27,35].

The initial charge and discharge curves at 0.1 C rate of the half-cell (1 C = 250 mA g$^{-1}$) are shown in Fig. 4a. A small discharge platform around 2.8 V for L@S, which can also be seen in the differential capacity-voltage curves (Fig. 4b) and CV plots (Fig. S6a, b), is ascribed to spinel discharge characteristic [20,36]. Specifically, the discharge capacities of LMNC and L@S electrodes are 294.9 and 292.6 mA h g$^{-1}$, respectively. It is worth noting that the capacity ratio slightly reduces near the 4.5 V plateau (Table S2), which is ascribed to the pre-activation of a portion of Li$_2$MnO$_3$ phase resulting from the introduced oxygen vacancies [25]. The release of oxygen was suppressed during the electrochemical activation of Li$_2$MnO$_3$. In addition, the coated spinel layer could also protect the surface of electrode from the corrosion of HF and then hinder the side reactions [31]. As a result, L@S cathode shows one of the highest initial Coulombic efficiency of
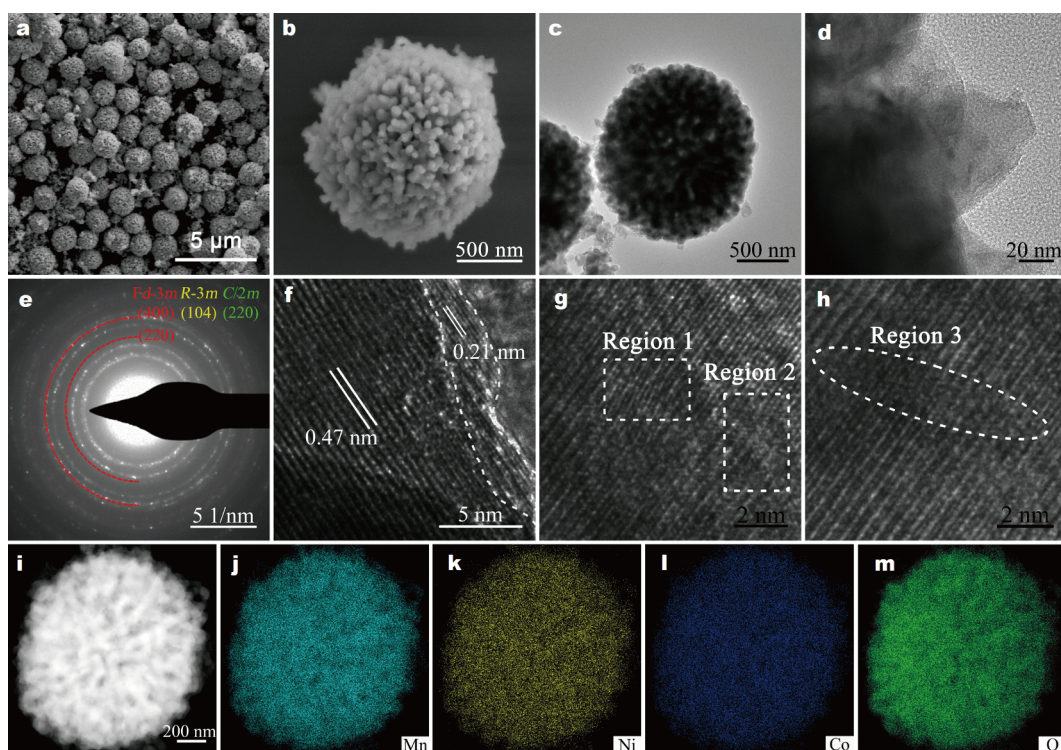
**Figure 3** (a, b) SEM, (c, d) TEM images; (e) SAED pattern, (f–h) HRTEM images, HAADF image (i) and the corresponding element mappings of (j) Mn, (k) Ni, (l) Co, (m) O for L@S.

92.3% when compared to other cathode materials reported previously (Table S3) [5,12,31,37–42].

L@S cathode delivers a reversible capacity of 226 mA h g$^{-1}$ after 200 cycles at 1 C (Fig. S6c), whereas that of pristine LMNC is 212 mA h g$^{-1}$. As shown in Fig. 4c, the L@S exhibits a high discharge capacity of 225 mA h g$^{-1}$ with a high capacity retention of 85.2% after cycling 200 times at 5 C. While the capacity of LMNC cathode under the same condition decays from 232 to 179 mA h g$^{-1}$. Such high specific capacity and good cycling performance of L@S cathode should be attributed to the following aspects. First, the introduced oxygen vacancies play a positive role in facilitating the diffusion of Li$^+$ [21,22]. Second, the *in-situ* formed surface spinel encapsulating layer with 3D Li$^+$ diffusion channels benefits Li$^+$ transportation between the layered host and the electrolyte. Finally, L@S cathode material shows better structural stability than pristine material. The SEM images (Fig. S7) of the cycled cathode materials directly prove that the spinel-modified layer can greatly hinder the formation of solid electrolyte interface on L@S electrode.

As shown in Fig. 4d, the average reversible specific capacities at 0.2, 0.5, 1, 2, 3, 4, 5 and 10 C are 290, 283,

275, 267, 263, 256, 249 and 221 mA h g$^{-1}$, respectively, whereas those of LMNC are 285, 273, 257, 238, 225, 212, 202 and 170 mA h g$^{-1}$. Obviously, L@S achieves higher discharge capacities at various current rates than LMNC counterpart. Typically, the L@S delivers a very high discharge capacity of 249 mA h g$^{-1}$ at 5 C, which is 86.2% of that at 0.2 C. In contrast, the LMNC has a capacity of 202 mA h g$^{-1}$ at the same rate, corresponding to 70.9% of that at 0.2 C. In addition, when the current density returns to 0.2 C, the specific capacity of LMNC is 271 mA h g$^{-1}$, which is 95% of the initial capacity. Under the same conditions, the reversible specific capacity of L@S reaches 283 mA h g$^{-1}$, 98% of the initial capacity, evidencing better rate capability of L@S cathode. As shown in Fig. 4e, the fabricated L@S cathode possesses one of the most outstanding rate capability among other Li-rich cathode materials reported previously [5,22,27,31,37–43]. Fig. 4f shows the long-term cyclic stability of L@S cathode at ultrahigh current rates. L@S has a discharge capacity of 222 mA h g$^{-1}$ with a capacity retention of 95.7% after 100 cycles at 10 C. When the current rate further increases to 20 C, L@S can still deliver a reversible capacity of 153 mA h g$^{-1}$ after 100 cycles, which is much better than LMNC (Fig. S6d). By contrast,
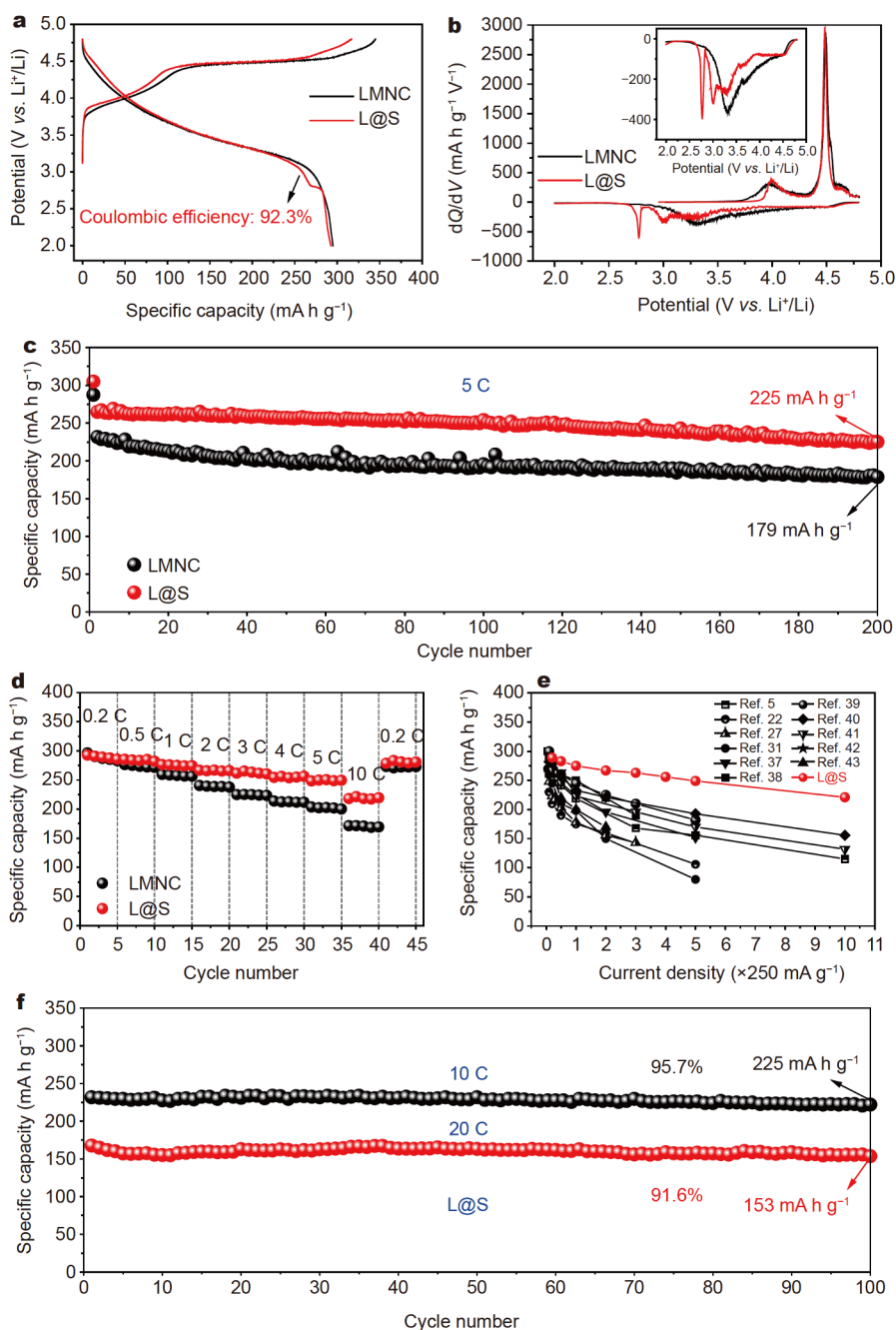
**Figure 4** (a) Initial charge/discharge curves at 0.1 C for LMNC and L@S. (b) The corresponding differential capacity *versus* voltage (dQ/dV) plots of initial cycle for LMNC and L@S. The inset in (b) shows the enlarged dQ/dV curves for the discharge process. (c) Discharge-cycling performances of both samples at 5 C. (d) Rate performances of LMNC and L@S. (e) Comparison of rate performances among L@S and other Li-rich cathode materials. (f) Discharge-cycling performances of L@S at 10 and 20 C.

besides the porous structure facilitating the penetration of electrolyte, the superior rate performances and cycling stability of L@S mainly benefit from the introduced oxygen vacancies and the surface spinel encapsulating layer.

The Nyquist plots of LMNC and L@S before cycling and equivalent circuit models are shown in Fig. 5a. In the high-frequency zone, the intercept on the real axis represents the ohmic impedance of the solution ($R_e$). The semicircle in the high-to-medium frequency region is

ascribed to the impedance of charge transfer ($R_{ct}$) at the interface between electrode and electrolyte. The straight line in the low frequency is due to the $Li^+$ diffusion in the solid electrode material. For L@S cathode, an additional semicircle appears in the low frequency region, which is caused by the diffusion of $Li^+$ in the spinel layer ($R_{spinel}$). According to the electrochemical impedance spectra, the calculated diffusion coefficients ($D_{Li}^+$) of the L@S and LMNC electrodes are $4.58 \times 10^{-16}$ and $3.62 \times 10^{-18}$ $cm^2$ $s^{-1}$, respectively, confirming the enhanced $Li^+$ diffusion kinetics of L@S (Fig. 5b and Table S4). The main factor is that the oxygen vacanies would lead to an imbalanced charge distribution and thus the formation of local electric fields, which is beneficial to the ionic/electronic transport [21]. Furthermore, the spinel phase with 3D channels has a higher $Li^+$ ions diffusion coefficient, and the porous structure of cathode material can shorten the diffusion distance of $Li^+$. As a result, the accelerated diffusion rate of $Li^+$ ions and the shortened transport paths both contribute to the enhanced diffusion kinetics of lithium ions and rate performances.

*In situ* XRD was carried out at 0.5 C (Fig. 5c, d). At the beginning of the initial charge process, (003) peak shifts to a low angle until the voltage reaches 4.5 V, indicating that the *c* increases continuously, due to the increased electrostatic repulsion between the adjacent lattice oxygen layers after $Li^+$ extraction from the lithium layers [31,37]. Then, during the charging plateau at 4.5 V, this peak shifts slightly back to high angle where $Li^+$ ions deintercalate from the transition metal layers. When further charged to 4.8 V, (003) peak sharply displaces to right, meaning the drastic decrease of *c*. This phenomenon is caused by the accelerated extraction of $Li^+$ from the transition metal layers and the irreversible oxygen loss [31]. During the discharge process, the peak shifts sharply toward low angle and then slowly returns to the right at the end. The turning point of this process is around 3.8 V. Before the turning point, the insertion of $Li^+$ ions into the lithium layers causes the increase of *c* parameter. After that, the continuously inserting of $Li^+$ into the vacancies in the crystal lattice, especially in the transition metal layers, would reduce the electrostatic repulsion between the oxygen layers, thus resulting in the decrease of *c* [44]. The variation of (003) peak during the 2nd cycle is analogous to that in the initial cycle, showing the similar mechanism. Notably, L@S has more dramatical (003) peak shifting than LMNC counterpart, revealing the deeper $Li^+$ insertion-extraction during cycling and being responsible for its higher reversible capacity. Furthermore, the more obvious recovery behavior of peak
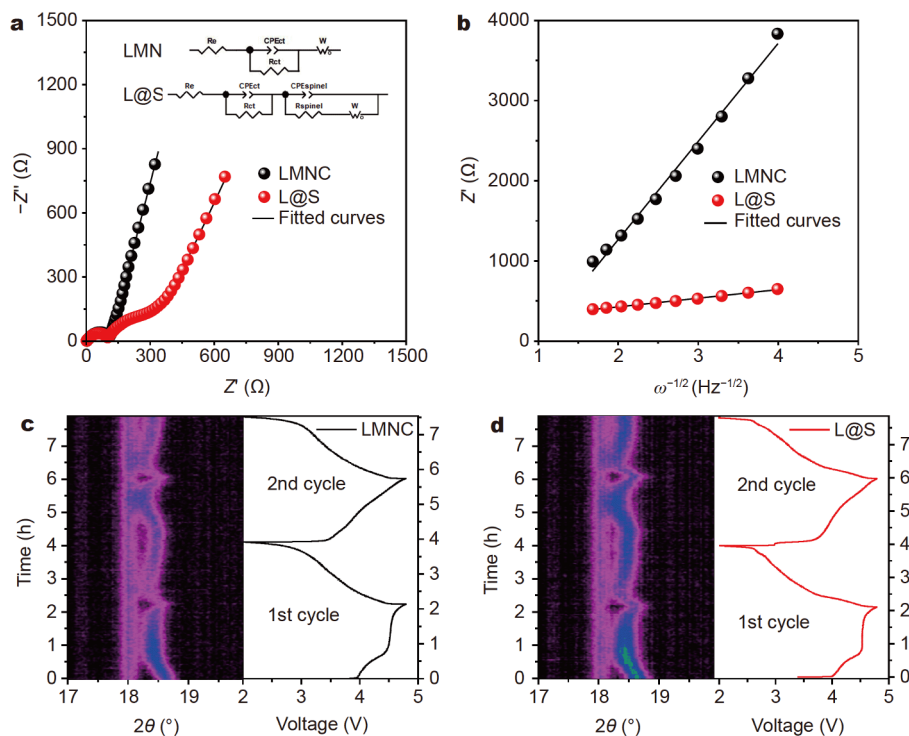


**Figure 5** (a) Nyquist plots of LMNC and L@S before cycling. The insets in (a) are equivalent circuit models. (b) The relationship between $Z'$ and $\omega^{-1/2}$ at low frequency region of corresponding EIS spectra. Color-coated images of the (003) peak of LMNC (c) and L@S (d).
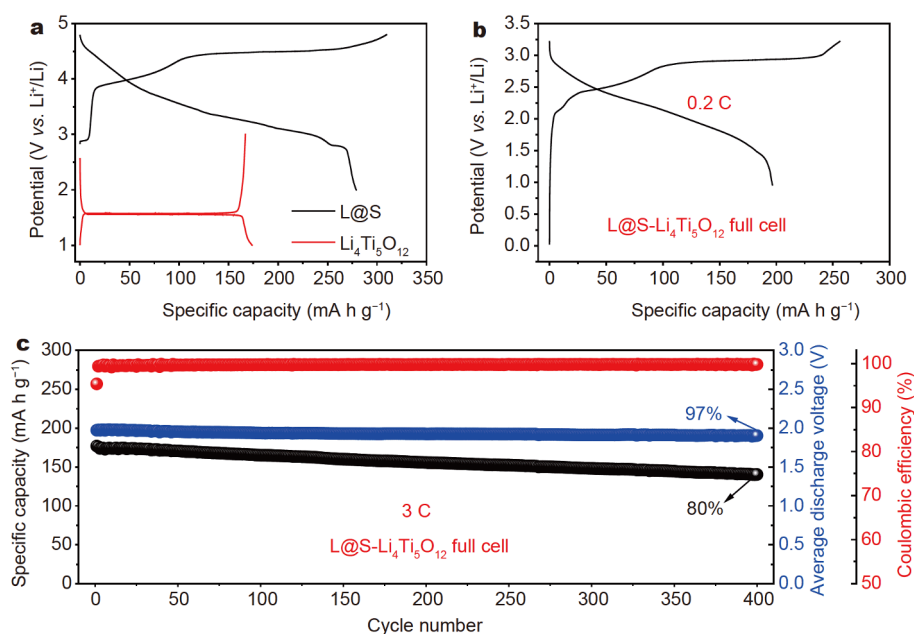
**Figure 6** Initial charge and discharge curves at 0.2 C of (a) L@S and $Li_4Ti_5O_{12}$ and (b) the full cell with L@S cathode and $Li_4Ti_5O_{12}$ anode. (c) Cycle performances of the full cell cycled between 0.96 and 3.22 V at 3 C.

shifting for L@S evidences its more stable structure, which is closely related to the surface spinel encapsulating layer.

Full cells with L@S as cathode and $Li_4Ti_5O_{12}$ as anode were constructed to demonstrate the superior lithium storage performance. $Li_4Ti_5O_{12}$ anode in the half-cell delivers a discharge capacity of 173 mA h g$^{-1}$ with a voltage plateau of 1.55 V at 0.2 C (Fig. 6a). After assembled into full cell, L@S has an initial discharge capacity of 197 mA h g$^{-1}$ at 0.2 C (Fig. 6b). As shown in Fig. 6c, a relatively high reversible specific capacity of 141 mA h g$^{-1}$ can be achieved after 400 cycles at a large current density 3 C, indicating excellent long-term high-rate cyclability. Interestingly, the discharge average voltage barely decays with a high retention of 97%. The excellent electrochemical properties of L@S cathode make it hold great potential for the practical application in high performance lithium ion batteries.

## CONCLUSIONS

In summary, a facile strategy has been proposed to introduce oxygen vacancies into hierarchically porous LMNC microspheres encapsulated by *in situ* formed surface spinel layer. The hierarchical porous configuration can shorten Li$^+$ diffusion paths. The introduced oxygen vacancies are not only able to pre-activate the lithium-rich phase, resulting in reduced irreversible ca-

pacity loss in the initial cycle, but also help to reduce the energy barrier of Li$^+$ diffusion. The resultant surface spinel encapsulating layer can prohibit the direct contact between electrode materials and electrolyte, and construct 3D Li$^+$ diffusion channels. As a result, L@S delivers a high initial Coulombic efficiency of 92.3% and a large discharge specficic capacity of 292.6 mA h g$^{-1}$ at 0.1 C. After 100 cycles at 10 C, an excellent reversible capacity of 222 mA h g$^{-1}$ with a capacity retention of 95.7% is obtained. Even at an extremely high rate of 20 C, L@S can deliver high and stable reversible capacity of 153 mA h g$^{-1}$. The full cell using L@S as cathode and $Li_4Ti_5O_{12}$ as anode exhibits a high capacity of 141 mA h g$^{-1}$ and outstanding voltage stability with a high retention of 97% after 400 cycles at 3 C. The effective multiscale coordinated design based on atomic defects, microstructure and composition may open up an insight to improve the lithium storage performance of lithium-rich layered oxides cathode materials.

1   Goodenough JB, Kim Y. Challenges for rechargeable Li batteries. Chem Mater, 2010, 22: 587–603
2   Tarascon JM, Armand M. Issues and challenges facing rechargeable lithium batteries. Nature, 2001, 414: 359–367
3   Xi LJ, Wang HE, Lu ZG, *et al.* Facile synthesis of porous LiMn$_2$O$_4$ spheres as positive electrode for high-power lithium ion batteries. J

*Power Sources*, 2012, 198: 251–257

4  Wang G, Liu H, Liu J, *et al.* Mesoporous LiFePO$_4$/C nanocomposite cathode materials for high power lithium ion batteries with superior performance. Adv Mater, 2010, 22: 4944–4948

5  Shi JL, Xiao DD, Ge M, *et al.* High-capacity cathode material with high voltage for Li-ion batteries. Adv Mater, 2018, 30: 1705575

6  Yu H, Zhou H. High-energy cathode materials (Li$_2$MnO$_3$–LiMO$_2$) for lithium-ion batteries. J Phys Chem Lett, 2013, 4: 1268–1280

7  Wang J, He X, Paillard E, *et al.* Lithium- and manganese-rich oxide cathode materials for high-energy lithium ion batteries. Adv Energy Mater, 2016, 6: 1600906

8  Yabuuchi N, Yoshii K, Myung ST, *et al.* Detailed studies of a high-capacity electrode material for rechargeable batteries, Li$_2$MnO$_3$−LiCo$_{1/3}$Ni$_{1/3}$Mn$_{1/3}$O$_2$. J Am Chem Soc, 2011, 133: 4404–4419

9  Yu X, Lyu Y, Gu L, *et al.* Understanding the rate capability of high-energy-density li-rich layered Li$_{1.2}$Ni$_{0.15}$Co$_{0.1}$Mn$_{0.55}$O$_2$ cathode materials. Adv Energy Mater, 2014, 4: 1300950

10 Chen M, Chen D, Liao Y, *et al.* Layered lithium-rich oxide nanoparticles doped with spinel phase: Acidic sucrose-assistant synthesis and excellent performance as cathode of lithium ion battery. ACS Appl Mater Interfaces, 2016, 8: 4575–4584

11 Qiu B, Yin C, Xia Y, *et al.* Synthesis of three-dimensional nanoporous Li-rich layered cathode oxides for high volumetric and power energy density lithium-ion batteries. ACS Appl Mater Interfaces, 2017, 9: 3661–3666

12 Zhang Y, Zhang W, Shen S, *et al.* Hollow porous bowl-shaped lithium-rich cathode material for lithium-ion batteries with exceptional rate capability and stability. J Power Sources, 2018, 380: 164–173

13 Chen Z, Yan X, Xu M, *et al.* Building honeycomb-like hollow microsphere architecture in a bubble template reaction for high-performance lithium-rich layered oxide cathode materials. ACS Appl Mater Interfaces, 2017, 9: 30617–30625

14 Cai Y, Huang SZ, She FS, *et al.* Facile synthesis of well-shaped spinel LiNi$_{0.5}$Mn$_{1.5}$O$_4$ nanoparticles as cathode materials for lithium ion batteries. RSC Adv, 2016, 6: 2785–2792

15 Yan P, Zheng J, Zhang X, *et al.* Atomic to nanoscale investigation of functionalities of an Al$_2$O$_3$ coating layer on a cathode for enhanced battery performance. Chem Mater, 2016, 28: 857–863

16 Zhang X, Belharouak I, Li L, *et al.* Structural and electrochemical study of Al$_2$O$_3$ and TiO$_2$ coated Li$_{1.2}$Ni$_{0.13}$Mn$_{0.54}$Co$_{0.13}$O$_2$ cathode material using ALD. Adv Energy Mater, 2013, 3: 1299–1307

17 Zhang S, Gu H, Tang T, *et al. In situ* encapsulation of the nanoscale Er$_2$O$_3$ phase to drastically suppress voltage fading and capacity degradation of a Li- and Mn-rich layered oxide cathode for lithium ion batteries. ACS Appl Mater Interfaces, 2017, 9: 33863–33875

18 Zheng F, Yang C, Xiong X, *et al.* Nanoscale surface modification of lithium-rich layered-oxide composite cathodes for suppressing voltage fade. Angew Chem Int Ed, 2015, 54: 13058–13062

19 Sun S, Yin Y, Wan N, *et al.* AlF$_3$ surface-coated Li[Li$_{0.2}$Ni$_{0.17}$Co$_{0.07}$Mn$_{0.56}$]O$_2$ nanoparticles with superior electrochemical performance for lithium-ion batteries. ChemSusChem, 2015, 8: 2544–2550

20 Liu J, Hou M, Yi J, *et al.* Improving the electrochemical performance of layered lithium-rich transition-metal oxides by controlling the structural defects. Energy Environ Sci, 2014, 7: 705–714

21 Xie Q, Liu P, Zeng D, *et al.* Dual electrostatic assembly of graphene encapsulated nanosheet-assembled ZnO-Mn-C hollow microspheres as a lithium ion battery anode. Adv Funct Mater, 2018, 28:

22 Qiu B, Zhang M, Wu L, *et al.* Gas–solid interfacial modification of oxygen activity in layered oxide cathodes for lithium-ion batteries. Nat Commun, 2016, 7: 12108

23 Wang G, Yi L, Yu R, *et al.* Li$_{1.2}$Ni$_{0.13}$Co$_{0.13}$Mn$_{0.54}$O$_2$ with controllable morphology and size for high performance lithium-ion batteries. ACS Appl Mater Interfaces, 2017, 9: 25358–25368

24 Zhang H, Wang J, Liu Q, *et al.* Extracting oxygen anions from ZnMn$_2$O$_4$: Robust cathode for flexible all-solid-state Zn-ion batteries. Energy Storage Mater, 2018

25 Ji Y, Li R, Mu D, *et al.* Surface modification of Li$_{1.2}$Mn$_{0.56}$Ni$_{0.16}$Co$_{0.08}$O$_2$ cathode material by supercritical CO$_2$ for lithium-ion batteries. J Electrochem Soc, 2018, 165: A2880–A2888

26 Liu D, Wang C, Yu Y, *et al.* Understanding the nature of ammonia treatment to synthesize oxygen vacancy-enriched transition metal oxides. Chem, 2019, 5: 376–389

27 Xu M, Fei L, Zhang W, *et al.* Tailoring anisotropic Li-ion transport tunnels on orthogonally arranged Li-rich layered oxide nanoplates toward high-performance Li-ion batteries. Nano Lett, 2017, 17: 1670–1677

28 Liu D, Zhang C, Yu Y, *et al.* Hydrogen evolution activity enhancement by tuning the oxygen vacancies in self-supported mesoporous spinel oxide nanowire arrays. Nano Res, 2017, 11: 603–613

29 Zhang L, Wang W, Jiang D, *et al.* Photoreduction of CO$_2$ on BiOCl nanoplates with the assistance of photoinduced oxygen vacancies. Nano Res, 2014, 8: 821–831

30 Yu Y, Shi Y, Zhang B. Synergetic transformation of solid inorganic–organic hybrids into advanced nanomaterials for catalytic water splitting. Acc Chem Res, 2018, 51: 1711–1721

31 Zhang XD, Shi JL, Liang JY, *et al.* Suppressing surface lattice oxygen release of Li-rich cathode materials *via* heterostructured spinel Li$_4$Mn$_5$O$_{12}$ coating. Adv Mater, 2018, 30: 1801751

32 Baddour-Hadjean R, Pereira-Ramos JP. Raman microspectrometry applied to the study of electrode materials for lithium batteries. Chem Rev, 2010, 110: 1278–1319

33 Zhao J, Huang R, Gao W, *et al.* An ion-exchange promoted phase transition in a Li-excess layered cathode material for high-performance lithium ion batteries. Adv Energy Mater, 2015, 5: 1401937

34 Yu R, Zhang X, Liu T, *et al.* Spinel/layered heterostructured Lithium-rich oxide nanowires as cathode material for high-energy lithium-ion batteries. ACS Appl Mater Interfaces, 2017, 9: 41210–41223

35 Fell CR, Qian D, Carroll KJ, *et al.* Correlation between oxygen vacancy, microstrain, and cation distribution in lithium-excess layered oxides during the first electrochemical cycle. Chem Mater, 2013, 25: 1621–1629

36 Xu M, Lian Q, Wu Y, *et al.* Li$^+$-conductive Li$_2$SiO$_3$ stabilized Li-rich layered oxide with an *in situ* formed spinel nano-coating layer: Toward enhanced electrochemical performance for lithium-ion batteries. RSC Adv, 2016, 6: 34245–34253

37 Xiao Z, Meng J, Li Q, *et al.* Novel MOF shell-derived surface modification of Li-rich layered oxide cathode for enhanced lithium storage. Sci Bull, 2018, 63: 46–53

38 Yu FD, Que LF, Wang ZB, *et al.* Controllable synthesis of hierarchical ball-in-ball hollow microspheres for a high performance layered Li-rich oxide cathode material. J Mater Chem A, 2017, 5: 9365–9376

39 Pang S, Xu K, Wang Y, *et al.* Enhanced electrochemical perfor-

mance of Li-rich layered cathode materials *via* chemical activation of Li$_2$MnO$_3$ component and formation of spinel/carbon coating layer. J Power Sources, 2017, 365: 68–75

40 Kim S, Cho W, Zhang X, *et al.* A stable lithium-rich surface structure for lithium-rich layered cathode materials. Nat Commun, 2016, 7: 13598

41 Li X, Zhang K, Mitlin D, *et al.* Fundamental insight into Zr modification of Li- and Mn-rich cathodes: Combined transmission electron microscopy and electrochemical impedance spectroscopy study. Chem Mater, 2018, 30: 2566–2573

42 Yu R, Zhang X, Liu T, *et al.* Hierarchically structured lithium-rich layered oxide with exposed active {010} planes as high-rate-capability cathode for lithium-ion batteries. ACS Sustain Chem Eng, 2017, 5: 8970–8981

43 Pei Y, Xu CY, Xiao YC, *et al.* Phase transition induced synthesis of layered/spinel heterostructure with enhanced electrochemical properties. Adv Funct Mater, 2017, 27: 1604349

44 Li X, Qiao Y, Guo S, *et al.* Direct visualization of the reversible O$^{2-}$/O$^-$ redox process in Li-rich cathode materials. Adv Mater, 2018, 30: 1705197

**Yuxin Cai** received his BE degree from the Department of Materials Science and Engineering, Shandong University. Currently, he is a ME candidate at the Department of Materials Science and Engineering in Xiamen University under the supervision of Prof. Lai-Sen Wang. His research focuses on the design and synthesis of high-performance cathode materials for lithium ion batteries.

**Lai-Sen Wang** is an Associated Professor in the Department of Materials Science and Engineering, College of Materials, Xiamen University. He received his PhD degree in materials physics and chemistry at Xiamen University in 2012. His research focuses on the electromagnetic transport property of thin films and the design and synthesis of nanocomposite materials for energy storage.

**Qingshui Xie** is an Associated Professor in the College of Materials, Xiamen University. He got his BSc and MSc degrees from Lanzhou University in 2009 and 2012, respectively. After that, he moved to Xiamen University as a PhD candidate and received his PhD degree in materials physics and chemistry in 2015. His research interest concentrates on the advanced electrode materials for high-performance lithium ion batteries.
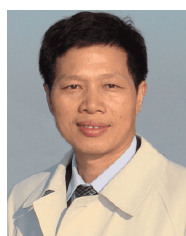
**Dong-Liang Peng** received his BSc (1983), MSc (1989) and PhD (1997) degrees in condensed matter physics from Lanzhou University. He received another PhD degree in materials science and engineering from Nagoya Institute of Technology (Japan) in 2002. Currently he is a Professor in the College of Materials, Xiamen University. He received the National Natural Science Fund for Distinguished Young Scholars. His research focuses on the nano functional materials, and their applications in catalysis, energy storage and electromagnetics.

## 氧空位提升锂离子电池富锂锰基正极分级多孔微米球的高倍率性能

蔡余新[1]，库伦[1]，王来森[1*]，麻亚挺[1]，郑鸿飞[1]，徐万杰[1]，韩江涛[1]，瞿佰华[2]，陈远志[1]，谢清水[1*]，彭栋梁[1*]

**摘要** 富锂锰基正极材料存在首次库仑效率低、倍率性能差以及电压衰减严重等问题，极大地限制了其规模化应用. 本文通过在富锂锰基分级多孔微米球的表面构筑氧空位(L@S)成功抑制了首次放电过程中不可逆Li$_2$O的形成，有效促进了Li$^+$离子的扩散动力学，从而提高了电极材料的结构稳定性. 研究结果表明，L@S正极在0.1 C电流密度下循环的首次库仑效率高达92.3%，放电比容量为292.6 mA h g$^{-1}$；在10 C大电流密度下循环100圈后可逆比容量为222 mA h g$^{-1}$，容量保持率为95.7%. 进一步增大电流密度至20 C时，循环100圈后L@S正极的放电比容量仍高达153 mA h g$^{-1}$. 此外，匹配Li$_4$Ti$_5$O$_{12}$负极组装的全电池在3 C电流密度下循环400圈后的可逆比容量为141 mA h g$^{-1}$，电压保持率高达97%.